A Novel Sample Selection Method for Impervious Surface Area Mapping Using JL1-3B Nighttime Light and Sentinel-2 Imagery

Pengfei Tang, Peijun Du, *Senior Member, IEEE*, Cong Lin, Shanchuan Guo, and Lu Qie

***Abstract*—Urbanization has attracted wide and active interests due to the impact on regional sustainable development. As an important indicator of urbanization, impervious surface area (ISA) should be accurately monitored. In scenario of identifying ISA by supervised classification from satellite images, the training samples are usually labeled manually, which is highly labor-intensive and time-consuming. High-resolution nighttime light image provides a unique footprint of human activities and settlements which are strongly correlated with ISA. In view of this, a novel ISA training sample selection method is proposed by integrating the JL1-3B high-resolution nighttime light imagery and Sentinel-2 time series imagery, and the random forest is applied to classify ISA from Sentinel-2 imagery. The quality of the automatically selected samples was quantitatively validated. There were over three study areas, and the overall classification accuracies were above 97%, showing reliable and robust performance. Compared with conventional methods, the proposed approach achieves satisfactory results in separating bare land from ISA. This study provides a data fusion way which can automatically generate sufficient and high-quality training samples for ISA mapping, and suggests that high-resolution nighttime imagery could demonstrate a promising potential for urban remote sensing.**

***Index Terms*—Automatic sampling, high-resolution nighttime light imagery (NTL), impervious surface area (ISA), Sentinel-2 imagery, urban remote sensing (RS).**

I. Introduction

URBANIZATION is regarded as an essential trend of the Earth's terrestrial surface changes. Although the urban area only occupies a small portion of global land, it carries the majority of population, economy, and culture. Therefore, it is crucial to have a comprehensive understanding of urbanization considering its significant impacts on urban environments and sustainable development such as urban heat island [1], air pollution [2], urban flood dynamic [3], and environment degradation [4]. Usually, the process of urbanization can be reflected by the dynamic changes of impervious surface area (ISA). ISA is generally defined as the artificial material which the water cannot penetrate [5]. The ISA mainly contains the land cover types associated with transportation (e.g., street, pavement, and parking lot), buildings (e.g., commercial, residential, and industrial areas), and other construction land [5].

Currently, remote sensing (RS) technology has shown enormous potential to detect ISA since it can provide accurate information on the Earth's surface spatially and temporally [6]. Many methods have been proved efficient for extracting ISA from multisource satellite images, and spectral indices show apparent advantages due to the easy implementation and convenience [7]. At present, a series of indices have been presented and applied to extract ISA including the normalized difference built-up index (NDBI) [8], normalized difference impervious surface index [9], biophysical composition index (BCI) [10], combinational build-up index [7], and others. Although these spectral indices can effectively enhance the ISA information, several problems still exist, especially the confusion between ISA and bare land which causes the false detection results of ISA extraction. Besides, the spectral indices are sensitive to image seasonality, thereby limiting observed time of the selected RS images [7].

Compared with the spectral indices, supervised classification possesses the advantage of separating ISA from spectral-similar pervious surfaces (e.g., bare land). By selecting the training samples and classifiers, supervised classification can classify the ISA from satellite images. However, the results of supervised classification strongly depend on the quality of training samples in terms of their representativeness and completeness [11], [12]. The generation of training samples is usually through screen digitalization in high-resolution imagery manually, in which the operator should have a comprehensive knowledge of land cover types for the study area [13]. Therefore, collecting sufficient training samples is a task which is highly labor-intensive and time-consuming, especially at a large scale [14].

By means of supervised classification framework, some global and regional land cover products released in recent years can be used to analyze ISA information as most of them have the land use type of ISA. For example, Gong *et al.* [15], [16] employed the Landsat and Sentinel-2 images to produce

Manuscript received April 26, 2020; revised June 5, 2020; accepted June 21, 2020. Date of publication June 24, 2020; date of current version July 16, 2020. This work was supported by the Natural Science Foundation of China under Grant 41631176. *(Corresponding author: Peijun Du.)*

Pengfei Tang, Peijun Du, Cong Lin, and Shanchuan Guo are with the Key Laboratory for Land Satellite Remote Sensing Applications of Ministry of Natural Resources, Nanjing University, Nanjing 210023, China, with the School of Geography and Ocean Science, Nanjing University, Nanjing 210023, China, and also with the Jiangsu Center for Collaborative Innovation in Geographical Information Resource Development and Application, Nanjing University, Nanjing 210023, China (e-mail: sgos_tpf@smail.nju.edu.cn; dupjrs@126.com; lcnjucumt@126.com; gsc@smail.nju.edu.cn).

Lu Qie is with the Key Laboratory of Coastal Zone Exploitation and Protection, Ministry of Natural Resources, Nanjing University, Nanjing 210023, China (e-mail: qielu@smail.nju.edu.cn).

This article has supplementary downloadable material available at https://ieeexplore.ieee.org, provided by the authors.

Digital Object Identifier 10.1109/JSTARS.2020.3004654

the Fine Resolution Observation and Monitoring of Global Land Cover product (FROM-GLC30 and FROM-GLC10). Chen *et al.* [17] produced the 30-m global land cover data product (GlobeLand30) for 2000 and 2010. Additionally, the European Space Agency (ESA) [18] developed the LandCover2009. Furthermore, there are also some global and regional high-resolution ISA products, such as the Global Urban Footprint (GUF) [19], High Resolution Layer Imperviousness Degree (HRL IMD) [20], Global Urban Land (GUL) [21], and Global Artificial Impervious Area (GAIA) [22]. However, though the above datasets are global products, they could not satisfy the current requirements of urban monitoring due to the low spatial resolution and limited accuracy in local region. Besides, these datasets have strong limitations in dynamic monitoring especially when cities are experiencing rapid urban sprawl, as it can only provide the distribution of ISA for certain years.

Nighttime light (NTL) imagery, providing a direct characteristic of human activity compared to daytime imagery, has also been applied to ISA estimation [23]. NTL imagery derived from multiple nighttime optical sensors can detect the light information which are closely related to human activities [24]. The common NTL sensors, including the Defense Meteorological Satellite Program's Operational Linescan System (DMSP-OLS), the Visible Infrared Imaging Radiometer Suite on the Suomi National Polar-orbiting Partnership satellite (NPP-VIIRS), and Luojia1-01 (LJ1-01), have been used in ISA extraction [25]–[27]. Although NTL image can acquire ISA information simply, it also has some limitations due to the blooming effect [28]. Fortunately, the integration of NTL data with daytime RS images are expected to solve this problem [29], [30]. Owing to the coarse spatial resolution of aforementioned NTL imagery, it is difficult to meet the requirements of fine ISA extraction. Recently, several advanced NTL satellites with high spatial resolution, such as EROS-B and Jilin 1-3B, have shown potential to refined mapping of ISA [23].

A few studies have been done to explore the relationship between the night lights of the high-resolution NTL imagery and land use or land cover [31]–[33]. Levin *et al.* [31] concluded that streets, commercial areas, and public service areas were the major sources of artificial light at night (ALAN) while agriculture land, rivers, and green space were dimly lit. Zheng *et al.* [33] concluded that in the JL1-3B NTL imagery of Hangzhou, major roads, commercial and institutional areas contributed most of the brightly lit pixels, while residential communities, industrial area, water body, and agricultural land were dimly lit at night. Although ALAN is strongly related to human activities, some ISA types (residential communities and industrial area) may be missed when ISA is extracted by using JL1-3B NTL imagery. Therefore, using brightly lit pixels as reliable impervious samples and then fusing the spectral features of optical images for ISA classification can effectively reduce the missed detection. However, few studies were conducted for ISA extraction using high-resolution NTL imagery as ancillary data through a classification approach based on fine spatial resolution RS imagery, such as Sentinel-2 multispectral (MS) imagery. This study presents a novel ISA extraction method by integrating the high-resolution NTL imagery and Sentinel-2 MS imagery. To achieve this aim, an automatic sample selection method for reliable training-samples generation is developed first, and random forest (RF) model is then established for ISA extraction based on features derived from Sentinel-2 optical data.

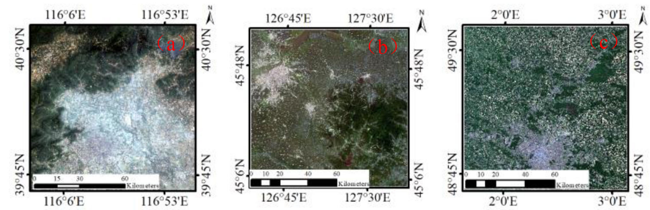

Fig. 1. Natural color composite image of study areas (Sentinel-2 images in which Band 4 = Red, Band 3 = Green, and Band 2 = Blue).

The rest of this article is structured as follows. Section II introduces the study areas and datasets. Section III presents the methodology of automatic sampling and classification. The proposed method is applied to the selected study areas; experimental results and comparisons with other methods are reported in Section IV. Finally, the conclusion is provided in Section V.

II. Materials

A. Study Area

Considering the data availability and urban properties, three cities, Beijing, Harbin, and Paris, are selected as study areas. Beijing (39.92° N, 116.46° E) is located in northern China, and has a monsoon-influenced humid continental climate [Fig. 1(a)]. Harbin (45.75° N, 126.68° E) is the provincial capital of Heilongjiang province, China. Harbin features a monsoon-influenced, humid continental climate [Fig. 1(b)]. Paris (48.52° N, 2.2° E), with a typical Western European oceanic climate [Fig. 1(c)]. Three cities have different geographic environments, climate conditions, and ISA distribution characteristics. These cities can be used to verify the applicability of the method under different experimental and complex surface coverage conditions.

B. Datasets and Preprocessing

1) Sentinel-2 Multispectral Data: Sentinel-2 time series images for three study areas in 2017 were acquired and used in sample selection and classification. The temporal resolution in this study is monthly interval. However, in some months, Sentinel-2 acquisitions have too much cloud cover (more than 10%), and eligible images of the near date are selected. Time series images were used because the presence/ absence of vegetation makes the pervious samples more difficult to be collected in a single Sentinel-2 image, and time series images are essential for collecting various pervious samples. Moreover, the classification performance is affected by acquisition date of the image. Thereby, time series images are essential for improving the classification accuracy. Table I shows the acquired time and cloud cover of the Sentinel-2 data which we used. Since Sentinel-2 Level-1 C products got from the European Space Agency (ESA) provide top-of-atmosphere (TOA) reflectance, this study uses the Sen2Cor processor to correct the effects

TABLE I
SENTINEL-2 IMAGE'S ACQUISITION DATES AND CLOUD COVER

	Jan/Cloud cover	Feb/Cloud cover	Mar/Cloud Cover	Apr/Cloud cover	May/Cloud cover	Jun/Cloud cover
Beijing	12-29/1.0301	02-27/0.0448	03-09/0.0893	04-18/0	05-28/0	06-27/0
Harbin	01-16/7.7608	02-15/1.002		04-16/0	05-26/1.166	06-15/1.4014
Paris	01-26/0	02-15/0.0072	03-27/7.0403	04-09/0	05-26/0	06-18/0

	Jul/Cloud cover	Aug/Cloud cover	Sep/Cloud cover	Oct/Cloud cover	Nov/Cloud cover	Dec/Cloud cover
Beijing	07-07/0.8705	08-06/1.8307	09-05/2.8075	10-05/0	11-24/0.0582	12-24/0.3585
Harbin	07-05/0.1621	07-25/0.1707	09-03/0.4096	09-23/7.5103	11-17/4.213	11-27/4.7436
Paris		08-14/18.589	08-27/5.8191	10-13/6.3702	11-22/0	

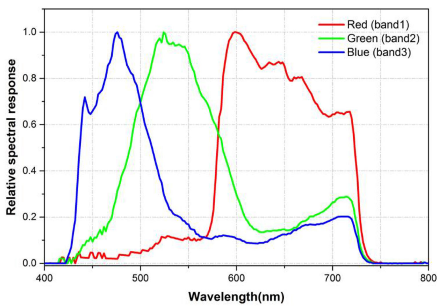

Fig. 2. Red-Green-Blue relative spectral response of the camera on the JL1-03 satellite.

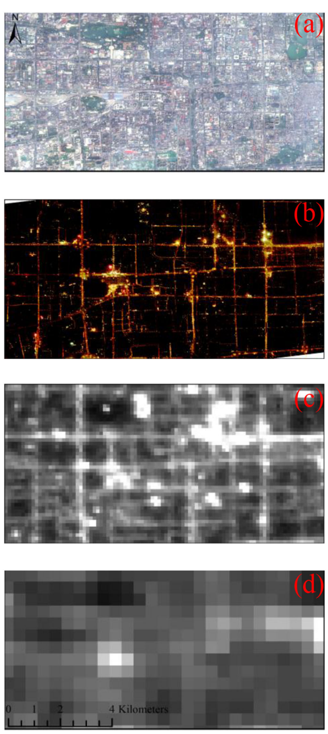

Fig. 3. Comparison of JL1-3B (b), Luojia1-01 (c) and NPP-VIIRS (d).

of the atmosphere to generate the Level-2 A products which provide the bottom-of-atmosphere (BOA) reflectance. The surface reflectance values are coded in JPEG2000 with the same quantification value of 10 000 as for Level-1 C products, so a factor of 1/10 000 was applied to Level-2 A digital numbers (DN) to retrieve surface reflectance values.

TABLE II
COMPARISON OF SOME SPACE-BORNE SENSORS FOR NTL IN BEIJING

Data	Acuquisition dates	Spatial resolution (m)
JL1-3B	2017/04/08	0.9
Luojia1-01	2018/11/23	130
NPP-VIIRS	2017/04	740

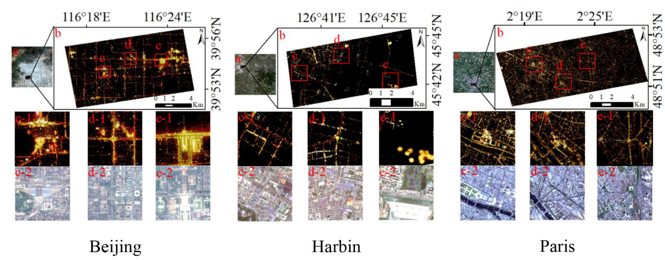

Fig. 4. Location of JL1-3B images. a is Sentinel-2 image. b is JL1-3B image. c-1, d-1, e-1 are the subsets of JL1-3B images and c-2, d-2, e-2 are the subsets of Sentinel-2 images.

2) Jinlin1-03B: The high-resolution NTL RS images for sample selection, are collected by a Chinese commercial satellite—Jinlin1-03B (JL1-3B) satellites. JL1-3B satellites, which are constructed and managed by Changguang Satellite Technology Co., Ltd. (CGSTCL), have a high spatial resolution of 0.92 m and a swath of 11 $\times$ 4.5 km. The data cover three bands: 430–512 nm (Blue), 489–585 nm (Green), and 580–720 nm (Red) [33]. Jilin 01 NTL RS imagery is the only public available submeter true color NTL image in the world, and the image can reflect the true color and intensity of the ground light in night time. The RGB relative spectral response of the camera on the JL1-03 satellite is shown in Fig. 2. Comparison of NPP-VIIRS, Luojia1-01, and JL1-3B is shown in Fig. 3. Table II displays some messages of space-borne sensors in Fig. 3. Three cloud-free scenes (April 8 for Beijing, March 20 for Harbin, and January 19 for Paris) were acquired for three study areas in 2017, with the overpass time of around 22:00 local time. Fig. 4 presents the location of JL1-3B image in the Sentinel-2.

The preprocessing of JL1-3B consists of four steps: the removal of background noises, radiometric calibration, the conversion of RGB images to grayscale brightness images, and the geometric correction and resampling. For each band of JL1-3B NTL data, a medium filter was used to eliminate outlier pixels and abnormally bright pixel [34]. Moreover, radiometric

TABLE III
PARAMETRIC FOR CONVERTING DN VALUE TO RADIANCE (W m^{-2} sr^{-1})

Parameters	a	b
R	9681.000	-4.730
G	5455.000	-3.703
B	2997.000	-4.471

calibration was applied on JL1-3B according to the document provided by CGSTCL. The conversion parameters (Table III) and a conversion equation between the DN value and the radiance of the three bands is [35]

$$L = (\mathrm{DN} - b)/a \tag{1}$$

where a and b are the corresponding parameters and L is the radiance in W m^{-2} sr^{-1} as the unit.

Then equation below was used to convert RGB images to the grayscale brightness images [36]

$$Brightness = 0.2989 \times Red + 0.5870 \times Green + 0.1140 \times Blue. \tag{2}$$

The $Brightness$ means the grayscale brightness of JL1-3B image, and Red, $Green$, and $Blue$ represent the radiance of the corresponding band.

After data preprocessing, for each JL1-3B image scene, approximately 30 accurate ground control points were manually collected for geometric correction. After geometric correction, JL1-3B NTL images are resampled to 10-m resolution by the nearest neighbor interpolation to match the Sentinel-2 image spatial resolution. The purpose of coarsening the spatial resolution is to reduce the effect of errors in spatial georeferencing and improve the correlations across sensors [37].

III. METHOD

A novel automatic sample selection method which takes advantage of both Sentinel-2 multispectral image (MSI) data and JL1-3B NTL data is proposed, and RF classifier is used for extracting ISA from Sentinel-2 multitemporal images. The workflow is illustrated in Fig. 5.

A. Automatic Sample Selection

Sentinel-2 time series images and JL1-3B NTL data are utilized to generate ISA samples. The sample selection method workflow is illustrated in Fig. 6. The specific processes are as follows.

1) For each temporal Sentinel-2 image, a pseudo sample pool P_m (m refers to the mth image) was constructed, based on spectral indices and NTL.
2) A criterion J was used to determine whether the P_m is suitable for producing the sample set T_m.
3) An iterative processing was designed to produce the T_m from the P_m when the J is satisfied. For each iteration, the disputed samples were detected and removed through an outlier detection algorithm until the stopping criteria S are met. The final sample set T was voted by the T_m.

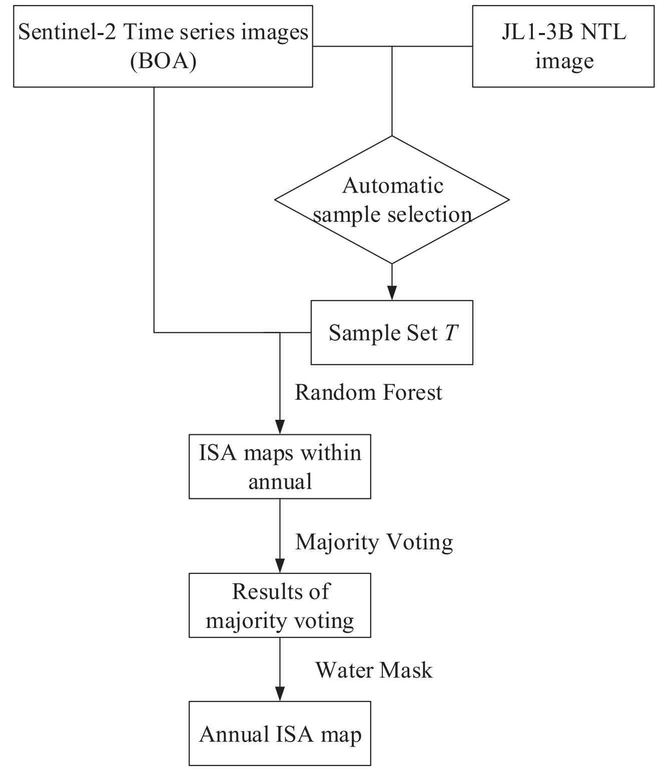

Fig. 5. Workflow of the proposed method.

1) Pseudo Sample Pool P: A pseudo sample pool P_m is illustrated in the flowchart in Fig. 7. Since water can reflect the moonlight and result in the error when performing geometric correction, the modified normalized difference water index (MNDWI) [38] and normalized difference vegetation index (NDVI) [39] were used in Sentinel-2 imagery to generate water and vegetation masks. The Otsu algorithm was used to determine the optimal thresholds (W_m and V_m in Fig. 7) for water and vegetation masks [40]. The Otsu algorithm is an adaptive threshold determination method and is widely used in image segmentation, which is identified by a discriminant criterion to maximize the separability of the resultant classes according to their gray levels. The threshold can be calculated and simply described as follows [11], [40]:

$$T = \arg\max \left[\omega_0 \omega_1 (\mu_1 - \mu_0)^2\right] \tag{3}$$

where T is the optimal threshold, ω_0 and ω_1 are the percentages of background pixels and target pixels in the image, respectively, and μ_0 and μ_1 are the mean values of the background pixels and target pixels, respectively.

The threshold for distinguishing NTL from background (g in Fig. 7) is considered as 89 $\mathrm{nW}/(\mathrm{cm}^2\mathrm{sr})$ [33]; pixels with the radiance value over 89 $\mathrm{nW}/(\mathrm{cm}^2\mathrm{sr})$ are considered as lit pixels, while the others are considered as background pixels. This threshold value was calculated when the DN value of the three bands is equal to 1 [37]. Thus, the impervious samples in P_m were selected by below rules: JL1-3B pixel radiance value should be over 89 $\mathrm{nW}/(\mathrm{cm}^2\mathrm{sr})$, meanwhile the value of MNDWI and NDVI in corresponding Sentinel-2 pixels should

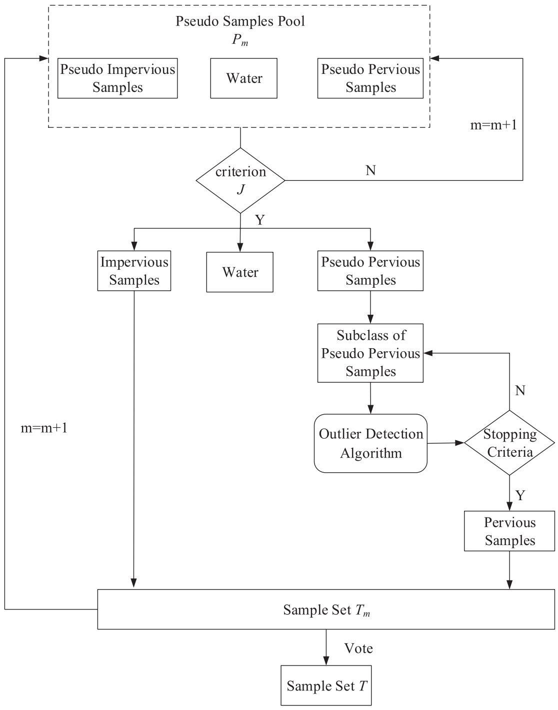

Fig. 6. Workflow of sample selection method.

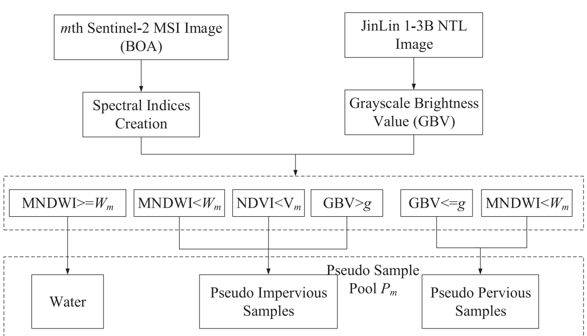

Fig. 7. Flowchart of pseudo sample pool.

be below W_m and V_m, respectively. The pixels with the highest radiance value of 89 $\mathrm{nW}/(\mathrm{cm}^2\mathrm{sr})$ in JL1-3B were regarded as the pseudo pervious samples. Water can be accurately identified by MNDWI; thus it was masked out from pseudo pervious samples. The pseudo impervious samples are retained. However, pseudo pervious samples which contain some ISA pixels that are not artificially lit (e.g., rooftops) need further processing.

2) Criterion J: Not all P_m are suitable to generate the training samples due to the seasonal variation of vegetation. Thus, in this part, a criterion J is defined to select appropriate P_m. In order to form J, some processing of P_m is as follows. First, for each pseudo class in P_m, a K-medoids algorithm was used to cluster into multiple subclasses. Owing to the high spectral variation, the pseudo impervious samples of P_m were clustered into two subclasses: high albedo and low albedo [41]; meanwhile the pseudo pervious samples were clustered into K subclasses including vegetation, bare land, ISA, and others by K-medoids [42]. The K-medoids algorithm is similar to K-means and is more robust to noises and outliers. Instead of using the mean of measurement in the subset, K-medoids uses a member of the subset which is called medoid to represent it. However, any other clustering algorithm can be used in this case. Next, the optimal value of K was identified by Calinski–Harabasz (CH) index [43], [44]. The index for n data points and K clusters is computed as follows:

$$CH = \left[\frac{\sum_{k=1}^{K} n_k \|z_k - z\|^2}{K-1}\right] \Bigg/ \left[\frac{\sum_{k=1}^{K}\sum_{i=1}^{N} \|x_i - z_k\|^2}{N-K}\right] \quad (4)$$

where the n_k is the number of points in cluster k, N is the number of entire data, z_k is the centroid of points in cluster, and z is the center of the entire data set [44]. Then, the Jeffries–Matusita (JM) distance was used to distinguish the separability between subclasses [45], [46]. The functions are given as follows [47], [48]:

$$J_{ij} = \sqrt{2(1 - e^{-b_{ij}})} \quad (5)$$

$$b_{ij} = \frac{1}{8}(\mu_i - \mu_j)^T \left(\frac{c_i + c_j}{2}\right)^{-1} (\mu_i - \mu_j) + \frac{1}{2}\ln\left(\left|\frac{|c_i + c_j|}{2\sqrt{|c_i| * |c_j|}}\right|\right) \quad (6)$$

where

b_{ij} was the Bhattacharyya distance between classes i and j, respectively.

c_i and c_j were the covariance matrices of classes i and j, respectively.

μ_i and μ_j were the mean vectors of classes i and j, respectively.

The JM distance ranges from 0 to 2; the higher the value, the higher the level of separability between the two classes [49]. Meanwhile, when JM distance is lower than 1, there is relatively low separability between the two classes [50]. For each P_m, the JM distances were calculated between subclasses of pseudo pervious samples and subclasses of pseudo impervious samples. The JM_{ij} refers to the JM distance between ith (i ranges from 1 to K) subclass of pervious samples and jth ($j = 1$ or 2) subclass of impervious samples.

Finally, the criterion J is as follows. For each *i*th subclass of pervious samples, if all JM_{ij} distance is lower than a threshold value which is supposed to be 1, it implies that the *m*th Sentinel-2 image is not suitable for producing ISA samples. Contrast, if the JM distance value in some subclasses of pervious samples and all subclasses of impervious samples is higher than 1, those subclasses will be retained for further process.

3) Outlier Detection Algorithm and Stopping Criteria: An iterative processing which contained an outlier detection algorithm was used to remove the ambiguous samples from the certain subclass of pervious samples, considering that single algorithm cannot effectively detect the samples that are similar to the impervious samples. The outlier detection algorithm which we used is a local outlier factor (LOF). LOF algorithm is a classical algorithm based on density, for finding anomalous data points by measuring the local deviation of a given data point with respect to its near neighbors [51]. The locality is given by k nearest neighbors, whose distance is used to estimate the density, and the points which have a substantially lower density than their neighbors will be considered to be outliers [52], [53]. And JM distance in each loop was recalculated between the new subclass of pervious samples and pseudo impervious samples, and the stopping condition is when JM distance maximizes.

The final sample set T was obtained by majority voting of the multitemporal sample set T_m, considering that the samples provided by a single period have seasonal variations.

B. Classification

Using the selected ISA samples as training data, RF classifier was trained and employed to produce the ISA maps from multitemporal Sentinel-2 images. RF is a well-known ensemble learning method which consists of many independent binary classification and regression trees (CART) [54]. For classification, each classifier contributes a single vote for the most frequent class to the input data. Then the RF outputs the class label which received the majority of votes [55]. RF has been widely applied to classify land cover and yield accurate land cover maps [16], [54]. The RF was chosen as the classifier for the following reasons. RF has yielded comparable results to the traditional support vector machine (SVM) method with a better tradeoff between the classification performances and the computational time [54]. More importantly, the RF is relatively robust to outliers and noise since the selected ISA samples may have some outliers [55].

In the classification procedure, to balance the computation efficiency and classification accuracy, 5000 pixels for each class were randomly selected from the automatically selected ISA sample set. Ten spectral bands, including four 10-m ground sampling distance bands [B2 (Blue), B3 (Green), B4 (Red), and B8 (Near infrared)] and six 20-m ground sampling distance bands [B5 (Red Edge 1), B6 (Red Edge 2), B7 (Red Edge 3), B8a (Red Edge 4), B11 (Short-wavelength infrared 1), and B12 (Short-wavelength infrared 2)] were stacked as the input features. The rest of the bands have less correlation to land cover differentiation as they mostly include the information which are relevant to atmosphere [56]. The final ISA map obtains by masking the water area on the multi-temporal classification results.

C. Accuracy Assessment

To evaluate the ISA classification accuracy, the ground reference data were collected through visual inspection of high-resolution images from Google Earth. To avoid spatial autocorrelation, evenly distributed validation samples were manually delineated for every study area, and each validation sample is limited to a maximum of 4 pixels. Moreover, the overall accuracy (OA) and Kappa index were employed to evaluate the classification accuracy. Furthermore, 100 training samples for each study were randomly selected to evaluate the correctness.

TABLE IV
SENTINEL-2 TASSELED CAP TRANSFORMATION (TCT) COEFFICIENTS FOR 6-BAND IMAGE

TCT	Blue	Green	Red	NIR-1	MIR-1	MIR-2
Brightness	0.3510	0.3813	0.3437	0.7196	0.2396	0.1949
Greenness	-0.3599	-0.3533	-0.4734	0.6633	0.0087	-0.2856
Wetness	0.2578	0.2305	0.0883	0.1071	-0.7611	-0.5308

IV. EXPERIMENTS AND RESULTS

A. Experimental Setup

1) Parameter Setting for the Proposed Method:

a) 5000 training pixels per class were randomly selected to implement the classification to balance the computational efficiency and classification accuracy.
b) Considering that the vegetation is sensitive to season, if the pervious samples appear more than once in T_m dataset, it will be defined as pervious samples in T dataset.
c) According to the previous study on RF [57], the number of trees (k) is 200 and the number of features were selected randomly at each node equal to the square root of total number of features ($m = \sqrt{p}$). In this study, p is 10; and then m is 3.

2) Compared to Other Methods: Two spectral indices (BCI and NDBI) and one land cover datasets (FROM-GLC10) were utilized to evaluate the performance of the presented method. The FROM-GLC10 was acquired by applying a training set which contains approximately 340 000 sample units of various sizes (from 30 × 30 m to 500 × 500 m) located at approximately 93 000 sites worldwide to Sentinel-2 images in 2017 with the RF classifier [16]. The FROM-GLC10 ISA product was extracted from FROM-GLC10 as it has a category of impervious surface. The formulas for the BCI [10] and NDBI [8] are given in

$$BCI = \frac{(TC_1 + TC_3)/2 - TC_2}{(TC_1 + TC_3)/2 + TC_2} \tag{7}$$

$$NDBI = \frac{SWIR - NIR}{SWIR + NIR} \tag{8}$$

where the TC_i ($i = 1, 2, 3$) are the normalized first three tasseled cap (TC) transformation components and the TC transformation coefficients for Sentinel-2 images are given in Table IV [58]. NIR refers to near infrared, MIR refers to middle infrared, and $SWIR$ refers to short-wavelength infrared.

For each temporal index image (NDBI or BCI), an optimal threshold was determined by Otsu algorithm for two-class segmentation (ISA/non-ISA). The final ISA map was produced by the majority of multitemporal ISA results when using spectral indices to estimate ISA.

B. Results of Automatic Sampling

As the Fig. 8 displays, the dark pixels in preproposed JL1-3B cannot be simply regarded as the pervious samples, since it contains large ISA. On the one hand, not all ISA are artificially lit in high-resolution NTL image, thus it cannot be selected as impervious samples. On the other hand, the dark pixels

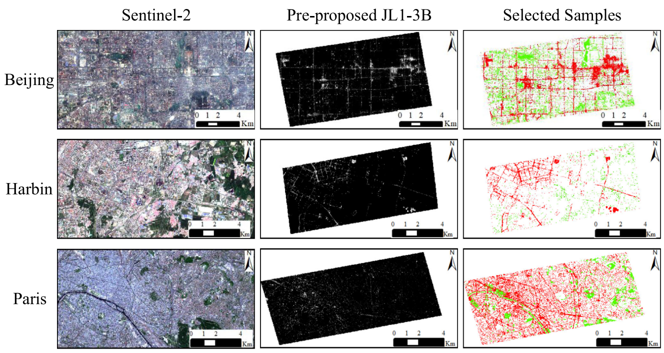

Fig. 8. Images and spatial distribution of selected samples—Red refers to impervious samples and Green refers to pervious samples, relatively.

TABLE V
SELECTED SAMPLE SIZE AND ACCURACY STATISTICS

	Number of pixels		Accuracy
Study area	Impervious	Pervious	OA (%)
Beijing	160378	126791	94
Harbin	46479	61995	99
Paris	171967	60463	90

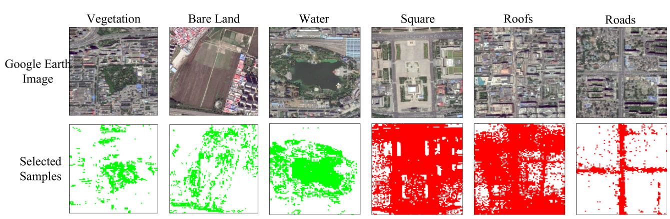

Fig. 9. Images and spatial distribution of selected samples. (Red refers to impervious samples; Green refers to pervious samples, relatively.).

in preproposed JL1-3B that are ISA were not considered as pervious samples through the iterative method. The quantity and quality of the selected samples are given in Table V.

From the quantity, our method can exploit the sufficient training samples by combining the JL1-3B and Sentinel-2 imagery. The impervious samples derived from JL1-3B NTL and Sentinel-2 imagery covered various ISA types; so were pervious samples. The impervious samples and pervious samples containing the land cover types are in Fig. 9.

From Figs. 8 and 9, the roof, road, and square were selected as impervious samples, while the vegetation, water, and bare land were selected as pervious samples. That is to say, the impervious samples extracted from the high-resolution NTL image and Sentinel-2 images had a diverse distribution which covered the urban and rural areas. Similarly, pervious samples not only contained the bare land in rural areas but also contained the lake and green space like park in urban areas. Sufficient quantity and good quality of the selected samples ensure that our method obtain satisfactory ISA results.

C. Results of ISA Extraction and Accuracy Assessment

The goal here is to examine the sample generation strategies which we proposed through classification performances. For this purpose, above 200 000 test pixels were selected randomly per

TABLE VI
CLASSIFICATION ACCURACY FOR FOUR METHODS

Area	Beijing		Harbin		Paris	
Accuracy index	OA(%)	Kappa	OA(%)	Kappa	OA(%)	Kappa
NDBI	75.74	0.5755	92.63	0.5803	88.65	0.5920
BCI	91.46	0.8342	90.88	0.5824	82.11	0.5014
FROMGLC-10	96.75	0.9336	96.76	0.8171	89.76	0.6333
Our method	97.14	0.9413	97.50	0.8580	97.56	0.9003

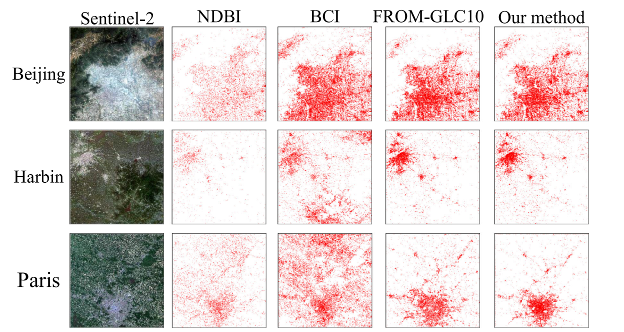

Fig. 10. ISA extraction results for four methods in three areas. (Red refers to ISA.)

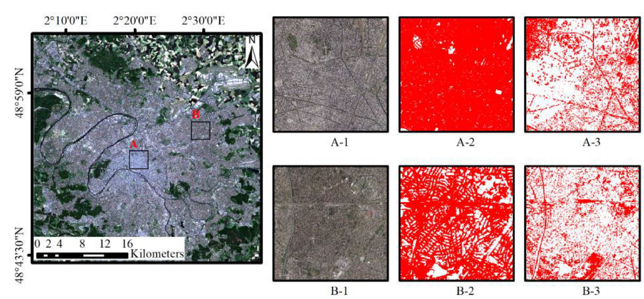

Fig. 11. Comparison of ISA extraction results in Paris using our method, FROM-GLC10, BCI in Paris: (A-1, B-1) Google Earth Image. (A-2, B-2) Our method. (A-3) FROM-GLC10. (B-3) BCI. (Red refers to ISA).

class (i.e., impervious and pervious classes) in three study areas. The accuracy assessment is displayed in Table VI and the ISA classification results are illustrated in Fig. 10.

From the accuracy assessment in Table VI, the OA was all above 97% and the Kappa was all above 0.85. Compared with other three strategies, our method achieved higher classification values in all study areas. In terms of visual inspection, our method has good performance in all three areas. It indicates that the high-resolution NTL image could be a reliable and effective source to generate the ISA training samples. From Fig. 10, the confusion between ISA and bare land is obvious in spectral indices methods. In BCI, some bare lands were misclassified into ISA class. Especially in Paris, the confusion is worse. On the contrary, the impervious class was misclassified into pervious class in NDBI. The confusion between ISA and bare land results in poorer performance by using BCI or NDBI strategies. In FROM-GLC10 ISA product, it has good accuracy both in Beijing and Harbin, however, the accuracy is poor in Paris.

As displayed in Fig. 11, the white area in A-3 mostly should have been the ISA; however, we found in FROM-GLC10 that it is bare land, indicating some ISA were confused with bare land,

TABLE VII
CLASSIFICATION ACCURACY ACROSS NINE AREAS USING FOUR METHODS

		NDBI		BCI		FROMGLC-10		Our method	
Area	Validation pixels	OA(%)	Kappa	OA(%)	Kappa	OA(%)	Kappa	OA(%)	Kappa
(1)-(a)	154	68.18	0.4787	92.21	0.8490	89.61	0.8013	94.81	0.8965
(1)-(b)	156	40.38	0.2892	89.10	0.7930	97.44	0.8456	95.51	0.9062
(1)-(c)	160	66.88	0.4948	93.13	0.8705	83.13	0.7076	97.43	0.9532
(2)-(a)	176	77.84	0.6305	83.52	0.7141	72.73	0.5643	96.02	0.9232
(2)-(b)	155	42.58	0.3067	88.39	0.7818	92.26	0.8469	96.13	0.9198
(2)-(c)	154	68.83	0.5030	85.06	0.7316	82.47	0.6912	98.70	0.9739
(3)-(a)	159	70.44	0.5502	83.65	0.7201	69.18	0.5351	88.05	0.7865
(3)-(b)	169	63.91	0.4190	88.17	0.7206	55.62	0.3517	91.12	0.7870
(3)-(c)	130	72.31	0.4851	63.08	0.4286	91.54	0.8176	84.62	0.6770

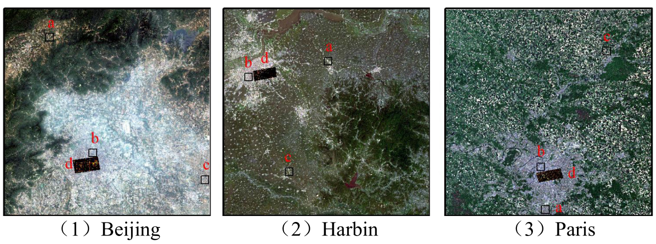

Fig. 12. Study areas: a, b, c for the areas away for the corresponding training area while d is the training area.

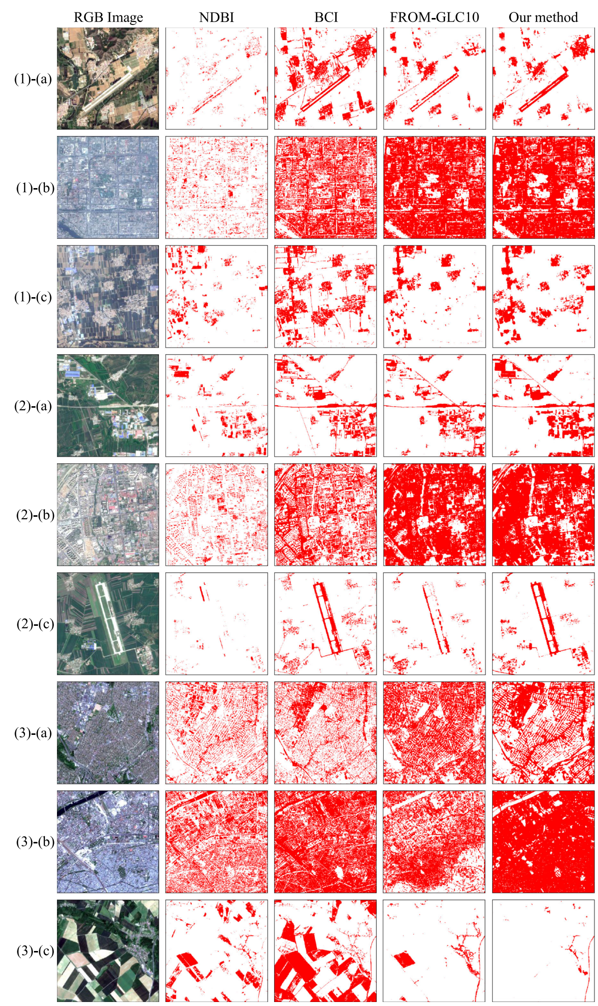

Fig. 13. Comparison of ISA results across nine areas using NDBI, BCI, FROM-GLC10, our method. The location of nine areas is shown in Fig. 12.

which results in the poor performance of FROM-GLC10 in Paris. Meanwhile, the impervious area and vegetation always mixed in area B, it will significantly decrease the BCI value. Because of this, the BCI has a bad performance in Paris. However, our method shows a good performs in both area A and area B, it demonstrates the ISA training samples extracted from JL1-3B can substantially cover the ISA types.

D. Examine the Method Over Different Areas

In order to examine the performance of four methods over different areas, nine areas which are away from the corresponding training area have been chosen. These areas contain downtown, rural residence land, airport, bare land, and region of badly mixed pixels. All areas are limited in size to 4 $\times$ 4 km. And some of these landscapes are similar to the training areas, while the others are different. The location of the selected areas and the detailed ISA extraction results are shown in Figs. 12 and 13, respectively. Moreover, accuracy assessment were conducted for these areas. The classification accuracy is in Table VII.

For the areas which are away from training areas, our method performs better than other three methods, which can be seen in Fig. 13 and Table VII. This again verifies the spectral indices method that can result in some bare lands being confused with ISA visually. Since the FROM-GLC10 land cover dataset is a global product, it has about 340 000 training samples with all types of land cover; hence, it performs well over the large areas [16]. However, in (1)-(a), (1)-(c), (2)-(a), (2)-(c), and (3)-(b) it omits some ISA. In our method, as Fig. 13 displays, the addition of distance from the training area does not influence classification performance. And from Figs. 11 and 13, our method can achieve good performance as long as the landscape remains similar to the training areas. But when the landscape has mixed pixels and is significantly different from that of the training area, there may be a few classification mistakes by using our method [e.g., (3)-(a) and (3)-(b)].

Mistakes always refer to missing some ISA when the landscape is widely different from the training areas. Especially in Paris, since the JL1-3B we used are in downtown of the city, the selected impervious training samples are all reliable ISA pixels. It may cause an underestimation of ISA in rural areas which has mixed pixels due to the 10-m spatial resolution of Sentinel-2 image. Due to the ISA has some special feathers in specific area, more impervious/pervious surface types can be derived by our method. So, in the overwhelming majority of cases, when the landscape is significantly different from that of the training area, our method still has excellent performance.

Since OA value is above 97% and Kappa index is above 0.85 in three study areas over the sentinel image, the high-resolution NTL image is effective in providing training samples for ISA mapping.

V. Conclusion

In this article, a new method had been developed to detect the ISA by joint use of the JL1-3B high-resolution NTL imagery and Sentinel-2 MSI time series imagery. With the proposed sample selection scheme, by the use of iterative processing and the time series spectral information and NTL brightness information, it is efficient to automatically select reliable and diverse training samples, which ensure the accuracy of classification results. Sequentially, using RF, all study areas have satisfactory classification accuracy and good visual effect, demonstrating the effectiveness of the proposed method. Compared to other three methods, our approach significantly avoids the confusion between the ISA and bare land, thus greatly improving the accuracy of the ISA extraction.

The proposed method has also been examined over different areas for detailed extraction results. The results reveal that the factor which affects the classification accuracy is the landscape of the area rather than the distance from the training area. That is to say, our method may omit certain ISA types, resulting in an underestimation of ISA in the large area. Besides, since the resolution of JL1-3B imagery is under 1.0 m, future works will be carried out to apply JL1-3B imagery with other high-resolution MS imagery (e.g., Gao-Fen) to detect the ISA.

References

[1] X. Li, Y. Zhou, G. R. Asrar, and Z. Zhu, “Creating a seamless 1km resolution daily land surface temperature dataset for urban and surrounding areas in the conterminous United States,” *Remote Sens. Environ.*, vol. 206, pp. 84–97, 2018. [Online]. Available: http://www.sciencedirect.com/science/article/pii/S0034425717305850

[2] A. G. Touchaei, H. Akbari, and C. W. Tessum, “Effect of increasing urban albedo on meteorology and air quality of montreal (Canada) - Episodic simulation of heat wave in 2005,” *Atmospheric Environ.*, vol. 132, pp. 188–206, 2016.

[3] G. Sofia, G. Roder, G. D. Fontana, and P. Tarolli, “Flood dynamics in urbanised landscapes: 100 years of climate and humans’ interaction,” *Sci. Rep.*, vol. 7, no. 1, 2017, Art. no. 40527. [Online]. Available: https://doi.org/10.1038/srep40527

[4] C. He, B. Gao, Q. Huang, Q. Ma, and Y. Dou, “Environmental degradation in the urban areas of China: Evidence from multi-source remote sensing data,” *Remote Sens. Environ.*, vol. 193, pp. 65–75, 2017. [Online]. Available: http://www.sciencedirect.com/science/article/pii/S003442571730086X

[5] Q. Weng, “Remote sensing of impervious surfaces in the urban areas: Requirements, methods, and trends,” *Remote Sens. Environ.*, vol. 117, pp. 34–49, 2012.

[6] H. Zhang, Y. Zhang, and H. Lin, “A comparison study of impervious surfaces estimation using optical and SAR remote sensing images,” *Int. J. Appl. Earth Observ. Geoinformation*, vol. 18, pp. 148–156, 2012. [Online]. Available: http://www.sciencedirect.com/science/article/pii/S0303243412000086

[7] G. Sun, X. Chen, X. Jia, Y. Yao, and Z. Wang, “Combinational build-up index (CBI) for effective impervious surface mapping in urban areas,” *IEEE J. Sel. Topics Appl. Earth Observ. Remote Sens.*, vol. 9, no. 5, pp. 2081–2092, May 2016.

[8] Y. Zha, J. Gao, and S. Ni, “Use of normalized difference built-up index in automatically mapping urban areas from TM imagery,” *Int. J. Remote Sens.*, vol. 24, no. 3, pp. 583–594, 2010.

[9] H. Xu, “Analysis of impervious surface and its impact on urban heat environment using the normalized difference impervious surface index (NDISI),” *Photogrammetric Eng. Remote Sens.*, vol. 76, no. 5, pp. 557–565, 2010. [Online]. Available: https://www.ingentaconnect.com/content/asprs/pers/2010/00000076/00000005/art00002 https://doi.org/10.14358/PERS.76.5.557

[10] C. Deng and C. Wu, “BCI: A biophysical composition index for remote sensing of urban environments,” *Remote Sens. Environ.*, vol. 127, pp. 247–259, 2012.

[11] C. Lin *et al.*, “Automatic updating of land cover maps in rapidly urbanizing regions by relational knowledge transferring from GlobeLand30,” *Remote Sens.*, vol. 11, no. 12, 2019, Art. no. 1397. [Online]. Available: https://www.mdpi.com/2072-4292/11/12/1397

[12] P. Du *et al.*, “Advances of four machine learning methods for spatial data handling: A review,” *J. Geovisualization Spatial Anal.*, vol. 4, no. 1, 2020, Art. no. 13. [Online]. Available: https://doi.org/10.1007/s41651-020-00048-5

[13] Z. Miao *et al.*, “Integration of satellite images and open data for impervious surface classification,” *IEEE J. Sel. Topics Appl. Earth Observ. Remote Sens.*, vol. 12, no. 4, pp. 1120–1133, Apr. 2019.

[14] C. Liu *et al.*, “Automated extraction of built-up areas by fusing VIIRS nighttime lights and Landsat-8 data,” *Remote Sens.*, vol. 11, no. 13, 2019, Art. no. 1571.

[15] P. Gong *et al.*, “Finer resolution observation and monitoring of global land cover: First mapping results with landsat TM and ETM+ data,” *Int. J. Remote Sens.*, vol. 34, no. 7, pp. 2607–2654, 2013. [Online]. Available: https://doi.org/10.1080/01431161.2012.748992

[16] P. Gong *et al.*, “Stable classification with limited sample: Transferring a 30-m resolution sample set collected in 2015 to mapping 10-m resolution global land cover in 2017,” *Sci. Bull.*, vol. 64, no. 6, pp. 370–373, 2019.

[17] J. Chen *et al.*, “Global land cover mapping at 30m resolution: A POK-based operational approach,” *ISPRS J. Photogrammetry Remote Sens.*, vol. 103, pp. 7–27, 2015. [Online]. Available: http://www.sciencedirect.com/science/article/pii/S0924271614002275

[18] S. Bontemps *et al.*, “GlobCover 2009-Products description and validation report,” vol. 2, 2011. [Online]. Available: http://ionia1. esrin. esa. int/docs/GLOBCOVER2009_Validation_Report_2

[19] T. Esch *et al.*, “Breaking new ground in mapping human settlements from space–The global urban footprint,” *ISPRS J. Photogrammetry Remote Sens.*, vol. 134, pp. 30–42, 2017. [Online]. Available: http://www.sciencedirect.com/science/article/pii/S0924271617301880

[20] C. Sannier, J. Gallego, J. Dahmer, G. Smith, H. Dufourmont, and A. Pennec, “Validation of copernicus high resolution layer on imperviousness degree for 2006, 2009 and 2012,” in *Proc. Int. Symp. Spatial Accuracy Assessment Natural Resour. Environ. Sci.*, 2016, pp. 5–8.

[21] X. Liu *et al.*, “High-resolution multi-temporal mapping of global urban land using Landsat images based on the Google Earth Engine platform,” *Remote Sens. Environ.*, vol. 209, pp. 227–239, 2018. [Online]. Available: http://www.sciencedirect.com/science/article/pii/S003442571830066X

[22] P. Gong *et al.*, “Annual maps of global artificial impervious area (GAIA) between 1985 and 2018,” *Remote Sens. Environ.*, vol. 236, 2020, Art. no. 111510. [Online]. Available: http://www.sciencedirect.com/science/article/pii/S0034425719305292

[23] N. Levin *et al.*, “Remote sensing of night lights: A review and an outlook for the future,” *Remote Sens. Environ.*, vol. 237, 2020, Art. no. 111443.

[24] J. Ou, X. Liu, P. Liu, and X. Liu, “Evaluation of Luojia 1-01 nighttime light imagery for impervious surface detection: A comparison with NPP-VIIRS nighttime light data,” *Int. J. Appl. Earth Observ. Geoinformation*, vol. 81, pp. 1–12, 2019.

[25] C. Small, F. Pozzi, and C. D. Elvidge, “Spatial analysis of global urban extent from DMSP-OLS night lights,” *Remote Sens. Environ.*, vol. 96, no. 3, pp. 277–291, 2005. [Online]. Available: http://www.sciencedirect.com/science/article/pii/S0034425705000696

[26] B. Yu *et al.*, “Urban built-up area extraction from log-transformed NPP-VIIRS nighttime light composite data,” *IEEE Geosci. Remote Sens. Lett.*, vol. 15, no. 8, pp. 1279–1283, Aug. 2018.

[27] Z. Yin, X. Li, F. Tong, Z. Li, and M. Jendryke, “Mapping urban expansion using night-time light images from Luojia1-01 and international space station,” *Int. J. Remote Sens.*, vol. 41, no. 7, pp. 2603–2623, 2019.

[28] M. Zhao *et al.*, “Applications of satellite remote sensing of nighttime light observations: Advances, challenges, and perspectives,” *Remote Sens.*, vol. 11, no. 17, 2019, Art. no. 1971.

[29] X. Liu, A. de Sherbinin, and Y. Zhan, “Mapping urban extent at large spatial scales using machine learning methods with VIIRS nighttime light and MODIS daytime NDVI data,” *Remote Sens.*, vol. 11, no. 10, 2019, Art. no. 1247.

[30] Z. Chen *et al.*, “Mapping global urban areas from 2000 to 2012 using time-series nighttime light data and MODIS products,” *IEEE J. Sel. Topics Appl. Earth Observ. Remote Sens.*, vol. 12, no. 4, pp. 1143–1153, Apr. 2019.

[31] N. Levin, K. Johansen, J. M. Hacker, and S. Phinn, “A new source for high spatial resolution night time images – The EROS-B commercial satellite,” *Remote Sens. Environ.*, vol. 149, pp. 1–12, 2014.

[32] Y. Katz and N. Levin, “Quantifying urban light pollution – A comparison between field measurements and EROS-B imagery,” *Remote Sens. Environ.*, vol. 177, pp. 65–77, 2016.

[33] Q. Zheng *et al.*, “A new source of multi-spectral high spatial resolution night-time light imagery-JL1-3b,” *Remote Sens. Environ.*, vol. 215, pp. 300–312, 2018.

[34] C. Elvidge, M. Zhizhin, K. Baugh, and F.-C. Hsu, “Automatic boat identification system for VIIRS low light imaging data,” *Remote Sens.*, vol. 7, no. 3, pp. 3020–3036, 2015.

[35] M. Du, L. Wang, S. Zou, and C. Shi, “Modeling the census tract level housing vacancy rate with the Jilin1-03 satellite and other geospatial data,” *Remote Sens.*, vol. 10, no. 12, 2018, Art. no. 1920.

[36] M. Grundland and N. A. Dodgson, “Decolorize: Fast, contrast enhancing, color to grayscale conversion,” *Pattern Recognit.*, vol. 40, no. 11, pp. 2891–2896, 2007.

[37] E. Guk and N. Levin, “Analyzing spatial variability in night-time lights using a high spatial resolution color Jilin-1 image–Jerusalem as a case study,” *ISPRS J. Photogrammetry Remote Sens.*, vol. 163, pp. 121–136, 2020. [Online]. Available: http://www.sciencedirect.com/science/article/pii/S0924271620300599

[38] H. Xu, “Modification of normalised difference water index (NDWI) to enhance open water features in remotely sensed imagery,” *Int. J. Remote Sens.*, vol. 27, no. 14, pp. 3025–3033, 2007.

[39] R. B. Myneni, F. G. Hall, P. J. Sellers, and A. L. Marshak, “The interpretation of spectral vegetation indexes,” *IEEE Trans. Geosci. Remote Sens.*, vol. 33, no. 2, pp. 481–486, Mar. 1995.

[40] N. Otsu, “A threshold selection method from gray-level histograms,” *IEEE Trans. Syst., Man, Cybern.*, vol. 9, no. 1, pp. 62–66, Jan. 1979.

[41] C. Wu and A. T. Murray, “Estimating impervious surface distribution by spectral mixture analysis,” *Remote Sens. Environ.*, vol. 84, no. 4, pp. 493–505, 2003.

[42] H.-S. Park and C.-H. Jun, “A simple and fast algorithm for K-medoids clustering,” *Expert Syst. Appl.*, vol. 36, no. 2, pp. 3336–3341, 2009.

[43] Y. Liu, Z. Li, H. Xiong, X. Gao, J. Wu, and S. Wu, “Understanding and enhancement of internal clustering validation measures,” *IEEE Trans. Cybern.*, vol. 43, no. 3, pp. 982–94, Jun. 2013. [Online]. Available: https://www.ncbi.nlm.nih.gov/pubmed/23193245

[44] C. Paris, L. Bruzzone, and D. Fernandez-Prieto, “A novel approach to the unsupervised update of land-cover maps by classification of time series of multispectral images,” *IEEE Trans. Geosci. Remote Sens.*, vol. 57, no. 7, pp. 4259–4277, Jul. 2019.

[45] L. Bruzzone, F. Roli, and S. B. Serpico, “An extension of the Jeffreys-Matusita distance to multiclass cases for feature selection,” *IEEE Trans. Geosci. Remote Sens.*, vol. 33, no. 6, pp. 1318–1321, Nov. 1995.

[46] Y. Chen, X. Zhao, and Z. Lin, “Optimizing subspace svm ensemble for hyperspectral imagery classification,” *IEEE J. Sel. Topics Appl. Earth Observ. Remote Sens.*, vol. 7, no. 4, pp. 1295–1305, Apr. 2014.

[47] J. A. Richards, “Feature reduction,” in *Remote Sens. Digi. Image Anl.*, Springer-Verlag, 2013, vol. 3, pp. 343–380.

[48] W. Hofmann, “Remote sensing: The quantitative approach,” *Earth-Sci. Rev.*, vol. 16, pp. 386–387, 1980. [Online]. Available: http://www.sciencedirect.com/science/article/pii/0012825280900896

[49] E. Adam and O. Mutanga, “Spectral discrimination of papyrus vegetation (*Cyperus papyrus L.*) in swamp wetlands using field spectrometry,” *ISPRS J. Photogrammetry Remote Sens.*, vol. 64, no. 6, pp. 612–620, 2009.

[50] P. Hao, Y. Zhan, L. Wang, Z. Niu, and M. Shakir, “Feature selection of time series MODIS data for early crop classification using random forest: A case study in Kansas, USA,” *Remote Sens.*, vol. 7, no. 5, pp. 5347–5369, 2015. [Online]. Available: https://www.mdpi.com/2072-4292/7/5/5347

[51] M. M. Breunig, H.-P. Kriegel, R. T. Ng, and J. Sander, “LOF: Identifying density-based local outliers,” in *Proc. ACM SIGMOD Int. Conf. Manage. Data*, 2000, pp. 93–104. [Online]. Available: https://doi.org/10.1145/342009.335388

[52] B. Chen *et al.*, “Ground and top of canopy extraction from photon-counting LiDAR data using local outlier factor with ellipse searching area,” *IEEE Geosci. Remote Sens. Lett.*, vol. 16, no. 9, pp. 1447–1451, Sep. 2019.

[53] B. Chen *et al.*, “Potential of forest parameter estimation using metrics from photon counting LiDAR data in Howland Research Forest,” *Remote Sens.*, vol. 11, no. 7, 2019, Art. no. 856.

[54] C. Pelletier, S. Valero, J. Inglada, N. Champion, and G. Dedieu, “Assessing the robustness of random forests to map land cover with high resolution satellite image time series over large areas,” *Remote Sens. Environ.*, vol. 187, pp. 156–168, 2016.

[55] V. F. Rodriguez-Galiano, B. Ghimire, J. Rogan, M. Chica-Olmo, and J. P. Rigol-Sanchez, “An assessment of the effectiveness of a random forest classifier for land-cover classification,” *ISPRS J. Photogrammetry Remote Sens.*, vol. 67, pp. 93–104, 2012. [Online]. Available: http://www.sciencedirect.com/science/article/pii/S0924271611001304

[56] C. Qiu, L. Mou, M. Schmitt, and X. X. Zhu, “Local climate zone-based urban land cover classification from multi-seasonal Sentinel-2 images with a recurrent residual network,” *ISPRS J. Photogramm. Remote. Sens.*, vol. 154, pp. 151–162, 2019. [Online]. Available: https://www.ncbi.nlm.nih.gov/pubmed/31417230

[57] Z. Xu, J. Chen, J. Xia, P. Du, H. Zheng, and L. Gan, “Multisource earth observation data for land-cover classification using random forest,” *IEEE Geosci. Remote Sens. Lett.*, vol. 15, no. 5, pp. 789–793, May 2018.

[58] T. Shi and H. Xu, “Derivation of tasseled cap transformation coefficients for Sentinel-2 MSI at-sensor reflectance data,” *IEEE J. Sel. Topics Appl. Earth Observ. Remote Sens.*, vol. 12, no. 10, pp. 4038–4048, Oct. 2019.

Pengfei Tang received the B.S. degree from School of Geoscience and Info-Physics, Central South University, Changsha, China, in 2018. He is currently working toward the Ph.D. degree in cartography and geographic information system with Nanjing University, Nanjing, China.

His research interests include image processing, and time-series image analysis.

Peijun Du (Senior Member, IEEE) received the Ph.D. degree in geodesy and survey engineering from China University of Mining and Technology, Xuzhou, China, in 2001.

He is currently a Professor of Remote Sensing and Geographical Information Science with Nanjing University, Nanjing, China. He has authored or coauthored more than 70 articles in international peer-reviewed journals, and more than 100 papers in international conferences and Chinese journals. His research interests include remote sensing image processing and pattern recognition, hyperspectral remote sensing, and applications of geospatial information technologies.

Dr. Du is an Associate Editor for IEEE GEOSCIENCE AND REMOTE SENSING LETTERS. He also served as the Cochair of the Technical Committee of the 5th IEEE GRSS/ISPRS Joint Workshop on Remote Sensing and Data Fusion over Urban Areas (URBAN 2009), International Association for Pattern Recognition (IAPR)-Workshop on Pattern Recognition in Remote Sensing (PRRS) 2012, International Workshop on Earth Observation and Remote Sensing Applications (EORSA) 2014, International Conference on Intelligent Earth Observing and Applications (IEOAs 2015), the Cochair of the Local Organizing Committee of Proceedings of Joint Urban Remote Sensing Event (JURSE) 2009, Workshop on Hyperspectral Image and Signal Processing (WHISPERS) 2012, and EORSA 2012, and the member of Scientific Committee or Technical Committee of other international conferences, including WHISPERS (2010–2016), URBAN (2011, 2013, and 2015), MultiTemp (2011, 2013, and 2015), International Symposium on Image and Data Fusion (ISIDF) 2011, and SPIE European Conference on Image and Signal Processing for Remote Sensing (2012–2016).

Cong Lin received the B.S. degree from the School of Environment Science and Spatial Informatics, China University of Mining and Technology, Xuzhou, China, in 2015. He is currently working toward the master's degree with the Jiangsu Provincial Key Laboratory of Geographic Information Science and Technology, Nanjing University, Nanjing, China.

His research interests include image processing, transfer learning, and scene classification

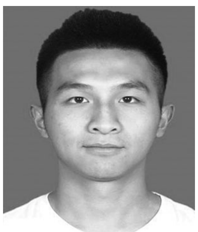

Shanchuan Guo received the M.S. degree in land resource management from the China University of Mining and Technology, Xuzhou, China, in 2018. He is currently working toward the Ph.D. degree with the School of Geography and Ocean Science, Nanjing University, Nanjing, China.

His research interests mainly include soil moisture retrieval, surface deformation monitoring from microwave remote sensing, and time series analysis.

Lu Qie received the B.S. degree in land resources management from Jilin University, Changchun, China, in 2018. She is currently working toward the Ph.D. degree in physical geography with Nanjing University, Nanjing, China.

Her research interests is in ecological effects of land use.